Chapter 8
Experimental Observations of Superlubricity and Thermolubricity

Martin Dienwiebel and Joost W.M. Frenken

Abstract The chapter introduces and discusses nanoscale effects called superlubricity and thermolubricity. Superlubricity is the phenomenon in which two surfaces slide over each other in dry contact without the atomic-scale instabilities. Superlubricity can reduce friction forces by orders of magnitude. Thermolubricity is the effect that thermal excitations significantly assist the contact between two bodies in overcoming the energy barriers against sliding, resulting in a reduction of the friction forces of contacts that are not superlubric.

8.1 Introduction

In this chapter we discuss manifestations of two effects, which we shall refer to as *superlubricity* and *thermolubricity*. Superlubricity is the phenomenon in which two surfaces slide over each other in dry contact without the atomic-scale instabilities that are thought to be the main source for energy dissipation. Superlubricity can reduce friction forces by orders of magnitude. Thermolubricity is the effect that thermal excitations significantly assist the contact between two bodies in overcoming the energy barriers against sliding, resulting in a reduction of the friction forces of contacts that are not superlubric. We shall argue that together, the two effects may lead to near-frictionless sliding over a wide range of conditions. Although we demonstrate these special effects for nanoscale contacts, we propose that they play

---

M. Dienwiebel (✉)
Karlsruhe Institute of Technology, Institute for Applied Materials—Reliability of Systems and Components, Microtribology Center µTC, Kaiserstr. 12, 76131 Karlsruhe, Germany
e-mail: martin.dienwiebel@iwm.fraunhofer.de

J.W.M. Frenken
Kamerlingh Onnes Laboratory, Leiden University, Im Schlehert 32, P.O. Box 9504, 2300 RA Leiden, The Netherlands

J.W.M. Frenken
Advanced Research Center for Nanolithography, Science Park 104, 1098 XG Amsterdam, The Netherlands
e-mail: frenken@physics.leidenuniv.nl

E. Gnecco and E. Meyer (eds.), *Fundamentals of Friction and Wear on the Nanoscale*, NanoScience and Technology, DOI 10.1007/978-3-319-10560-4_8

a key role in the well-known lubricating properties of some layered materials, such as graphite and molybdenum disulfide, and speculate they may hold a promise for further, low-friction applications.

8.1.1 The Transition to Frictionless Sliding in the One-Dimensional Case

In friction force microscopy (FFM) experiments at the atomic scale the lateral force signals often show a sawtooth-like modulation with the periodicity of the lattice of the substrate over which the tip is being moved. Observations of this type have been made on many different materials, such as graphite [1], mica [2], MoS_2 [3], copper [4], diamond [5, 6], and alkali-halides (NaF, NaCl, KF, KCl, KBr) [7–9]. The general characteristics of these observations are described well by a simple model that has been formulated first by Prandtl [10] and by Tomlinson [11]. Applied to the nanoscale geometry of a friction force microscope the model describes the motion of a point-like tip which is coupled by a spring to a moving support. The tip is in contact with a rigid solid, which is treated as a periodic potential energy surface. If this potential energy landscape has only a single Fourier component, with period a and amplitude V_0, we can write the lateral force on the tip as

$$\frac{2\pi}{a} V_0 \sin\left(\frac{2\pi}{a} x_t\right) = k(x_m - x_t) \tag{8.1}$$

where k is the stiffness of the spring and x_t and x_m denote the positions of the tip and the support.

The relative strength of the interaction potential with respect to the stiffness of the spring is often expressed in the form of a dimensionless parameter $\gamma \equiv 4\pi^2 V_0/ka^2$. When γ exceeds unity, multiple solutions exist to (8.1). The tip remains stuck in a metastable equilibrium position until the spring force is large enough to force the tip to rapidly slip to the next equilibrium position, which may again be merely metastable. These two elements, the sticking and the slipping, represent the stick-slip motion, commonly observed in FFM experiments. A tacit assumption in this description is that the excess potential energy that is released during the slip event is irretrievably lost to other degrees of freedom of the system, such as phonons in the substrate and the tip. As a consequence, stick-slip motion implies energy dissipation. By contrast with this scenario for energy dissipation, (8.1) predicts continuous sliding of the tip over the counter surface for $\gamma < 1$, i.e. when the surface potential is sufficiently weak and the spring is sufficiently stiff. In this case, the lateral force oscillates between negative (against the direction of attempted motion) and positive (forward) values and the average lateral force, i.e. the *friction* force, is zero. The transition from zero dissipation to non-zero friction at $\gamma = 1$, due to the breaking of analyticity, is known as an Aubry transition [12]. The Aubry transition has been investigated primarily in the context of the one-dimensional Frenkel-Kontorova model [12, 13], in which two one-dimensional lattices are sheared over each other. In this model, static friction and the Aubry transition depend strongly on the ratio p/q of the lattice constants of the top and bottom solid.

8.1.2 Superlubricity

The term *superlubricity* has been introduced by Hirano and Shinjo [14]. Originally, it was defined as the extension of the Aubry transition to a two-dimensional geometry and describes the effect that friction can vanish almost completely when two crystalline surfaces slide over each other in dry contact without wear and plastic deformation. This phenomenon was first demonstrated in a quasistatic calculation for rigid crystals with fcc, bcc and hcp symmetry and for various surface orientations [15]. In the two-dimensional case it was found that the frictionless or superlubric regime can be reached for a much wider range of values of γ and they noted that superlubricity should appear for any combination of flat and clean metals when the interaction potential is weak. Hirano and Shinjo concluded that a way to tune the interaction potential experimentally, is to change the commensurability between two surfaces. Of the theoretical work that has been performed after these first calculations we mention that by Sørensen et al. [16], who used molecular dynamics simulations to investigate friction at $T = 0\,\mathrm{K}$ between flat copper asperities, e.g. 19×19 atoms large, and a copper surface. When the asperity and the surface were both (111) oriented, the sliding did not involve wear. For an aligned contact, regular stick-slip motion was observed with high friction, whereas the friction force vanished when the contact was twisted 16.1° out of registry.

In this chapter, we will use the word superlubricity, even though it suggests an analogy between the *structural lubricity* at an incommensurate interface and the phenomena of superconductivity and superfluidity [17]. Lately, the term superlubricity has been used by several authors to also indicate other situations with extraordinarily low friction forces, not involving a lattice mismatch effect. Here, we will stick to the original meaning of the word and concentrate on experiments that probe the effect of commensurability on friction.

8.1.3 In Search for Superlubricity

In an early experiment, Hirano et al. [18] have employed a surface forces apparatus (SFA) to measure the orientation dependence of friction between mica sheets. They found a friction force of ($8 \times 10^{-4}\,\mathrm{N}$) when the orientations of the mica sheets matched. The friction force was reduced by as much as a factor 4 when the crystallographic directions of the mica sheets were misoriented relative to each other. Since in the incommensurate case friction was still relatively strong, either the superlubricity effect was incomplete or other mechanisms were responsible for additional channels of energy dissipation.

As was shown by Ko and Gellman [19], one such additional type of dissipation can be the internal friction that arises when the contact pressure is high enough to cause plastic deformation. These authors measured the friction force as function of the misfit angle between two Ni(100) crystal surfaces using an ultrahigh vacuum (UHV) tribometer and found a lower friction coefficient for 45° and 135° misfit angles than for 0° and other orientations. Although at first sight, this observation seems consistent with superlubricity, the orientational variations were still observed after adsorption of as much as 20 monolayers of ethanol or sulfur on the nickel surfaces prior to contact formation, which made Ko and Gellman conclude that the low friction in certain directions was caused by easy shearing along the preferred slip planes in the bulk. This explanation is consistent with the computer-simulation result obtained by Sørensen et al. [16] for shearing contacts between clean copper surfaces, which revealed that the shear occurred predominantly along the (111) planes, even for (001) oriented surfaces.

In another macroscopic experiment Martin et al. found a remarkably low friction coefficient between clean MoS_2 surfaces after a short sliding distance using a UHV tribometer [20]. After the experiment MoS_2 flakes were collected and examined with a transmission electron microscope (TEM). The TEM images showed that the flakes were rotated with respect to each other. The authors concluded that the low friction coefficient was due to the incommensurability between the flakes, thus due to superlubricity.

In 1997 Hirano et al. [21] have performed a scanning tunnelling microscope (STM) experiment and claimed the observation of superlubricity in UHV between a tungsten tip and a Si(001) surface. The tungsten tip was first imaged using field electron microscopy, after which it was advanced towards the Si surface until a tunnelling current could be measured. Since an STM is usually not capable of detecting forces, the bending of the tip was monitored optically and translated into a lateral force. When the major crystallographic axes of the two surfaces were aligned, a bending of the tungsten wire over an estimated 100 nm was measured, which was absent when the orientation was rotated over 45°.

8.2 Atomic-Scale Observation of Superlubricity

8.2.1 Commensurability-Dependent Superlubricity Between Finite Graphite Surfaces

In this chapter we concentrate on nanotribological experiments, conducted with a dedicated friction force sensor, the Tribolever [22]. This sensor is part of an unconventional friction force microscope [23] that allows quantitative tracking of the forces on the scanning tip in three directions, with a high resolution in the lateral forces, down to 15 pN. The instrument can rotate the sample to change the relative orientation between the tip and sample lattices. Initial measurements with this instrument have been performed on low-grade, highly oriented pyrolytic graphite (HOPG) [24, 25].

Although in some cases, these measurements showed traditional friction loops, with stick-slip character and measurable energy dissipation, in many friction loops the average friction force was very low and the tip was sliding over the graphite surface without stick-slip motion. Also it was found that the variation of the friction force with the normal force was rather weak. These observations strongly suggested that the sliding had been taking place between two graphite surfaces, one being the HOPG substrate, and the other being a small piece of graphite, i.e. a graphite flake, that was attached to the tungsten tip. The difference between the high- and low-friction force loops could then be attributed to the difference in commensurability between the flake and the substrate, high friction corresponding to a fully commensurate contact and low friction to an incommensurate contact.

In order to obtain further support for our interpretation of these initial observations, we have repeated the experiment much more carefully with a high-quality HOPG sample that had an average grain size of several millimeters. In the experiment we rotated this sample in small steps with respect to the tip. For each orientation, we performed a complete set of friction force spectroscopy measurements for a range of normal forces between +25 nN and pull-off (−22 nN) and a range of sliding directions. We recorded the lateral forces in the X- and the Y-direction of the sensor, from which we reconstructed the average friction force in the sliding direction (for details see [25]).

Figure 8.1 shows lateral force maps and force loops measured in the X-direction for different rotational orientations. A typical force loop is shown in Fig. 8.1d, which was measured at a normal force of 18 nN. The lateral force in Fig. 8.1d displays clearly resolved atomic-scale stick-slip sliding and the average friction force parallel to the sliding direction is 203.3 ± 20 pN. Figure 8.1b, e and c, f show FFM measurements obtained with the graphite substrate rotated +12° and −22° with respect to Fig. 8.1a, d around an axis normal to the surface and parallel to the tip. The rotation by 12° has caused the average friction force to reduce by more than one order of magnitude, to 15 ± 15 pN. Rotating 22° away from the first measurement in the opposite direction also has caused a reduction, to 8^{+16}_{-8} pN, which is equal to zero friction within the detection limit of our instrument. This variation of the friction force with the rotation angle Φ was completely reversible. Notice that the ultra-low lateral forces in Fig. 8.1e–f still exhibit regular variations with the periodicity of the graphite substrate.

Figure 8.2 displays the average friction forces measured over a 100° range of substrate rotation angles. We recognize two narrow angular regions with high friction, separated by a wide angular interval with nearly zero friction. The distance between the two friction peaks is 61 ± 2°, which corresponds well with the 60° symmetry of individual atomic layers in the graphite lattice. After every 60° rotation, the lattices of the substrate and the graphite flake align and the friction is high. For intermediate angles, the lattices are incommensurate and the friction force is close to zero.

The peak width in Fig. 8.2 can be used to estimate the flake diameter. For finite-size contacts, the cancellation of lateral forces, which causes superlubricity, can be

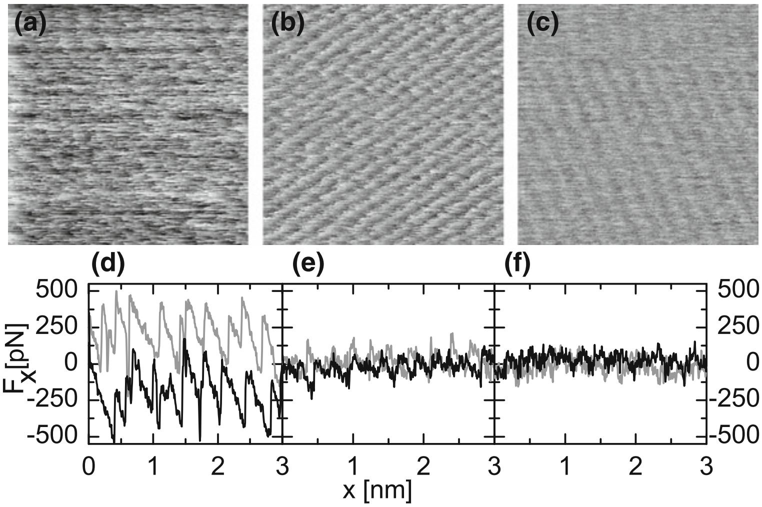

Fig. 8.1 Lateral force images (*forward direction*) and friction loops measured between a tungsten tip and a graphite substrate. The displayed signals correspond to the X-direction of the Tribolever sensor and rotation angles Φ of the graphite sample of 60° (**a**, **d**), 72° (**b**, **e**) and 38° (**c**, **f**). The normal force between the tip and the substrate amounted to $F_N = 18\,\text{nN}$ in (**a**, **d**) and (**c**, **f**) and $F_N = 30.1\,\text{nN}$ in (**b**, **e**). The grey scales in the force images cover force ranges of **a** 590 pN, **b** 270 pN, and **c** 265 pN. The image size is 3 nm × 3 nm. After [25]

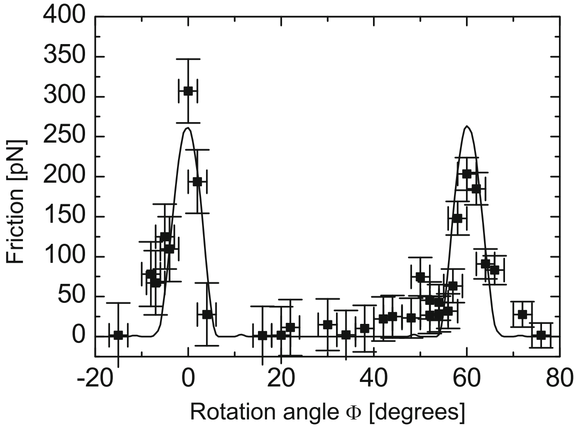

Fig. 8.2 Average friction force between a tungsten tip and a graphite substrate, plotted versus rotation angle Φ of the graphite sample with respect to an axis normal to the sample surface. Two *narrow peaks* of high friction are observed at 0° and 61°, respectively. Between these peaks a wide angular range with ultra-low friction, close to the detection limit of the instrument, is found. The first peak has a maximum friction force of 306 ± 40 pN, and the second peak has a maximum of 203 ± 20 pN. The curve through the data points shows results from a calculation according to the Tomlinson model for a symmetric 96-atom graphite flake sliding over the graphite surface (see text). After [25]

considered complete when the mismatch between the two lattices adds up to one lattice spacing over the diameter of the contact. The mismatch condition provides us with the estimate that $\tan(\Delta\Phi) = 1/D$, where $\Delta\Phi$ is the full width at half maximum of the friction peak, and D is the flake diameter, expressed in lattice spacings. From the widths of the two peaks in Fig. 8.2, of $5.4 \pm 1.0°$ for the first peak and $6.5 \pm 0.8°$ for the second, we estimate that the flake diameter is between 7 and 12 lattice spacings. The contact size was determined more precisely by Verhoeven et al. [26]. He modelled the flake as a rigid, finite lattice, with the hexagonal symmetry of a single layer of graphite. Because the relative positions of the atoms in the N-atom flake $(x_i, y_i, 0)$ with respect to the position (x_t, y_t, z_t) of the center of mass (CM) of the flake were fixed, the flake-surface interaction potential could simply be obtained by the summation over N atomic contributions:

$$\begin{aligned} V_{int}(x_t + x_i, y_t + y_i, z_t) = -V_0(z_t)[2\cos(b_1(x_t + x_i))\cos(b_2(y_t + y_i)) \\ + \cos(2b_2(y_t + y_i))] + V_1(z_t), \end{aligned} \tag{8.2}$$

with $b_1 = 2\pi/(0.246\,\text{nm})$ and $b_2 = 2\pi/(0.426\,\text{nm})$. The height-dependent corrugation amplitude per flake atom is given by $V_0(z)$, while $V_1(z)$ indicates the overall, i.e. N-atom position-averaged z-dependence of the interaction, expressed per atom. The amplitude of the summed potential depended strongly on the orientation angle Φ of the flake lattice with respect to the substrate lattice. The flake was coupled to a support by springs in the x- and y-directions (see Fig. 8.3), with which it was dragged through this N-atom interaction potential.

Symmetric flakes of various sizes were considered in the calculation. Each flake was a piece of graphene sheet and had a shape with 60° rotational symmetry.

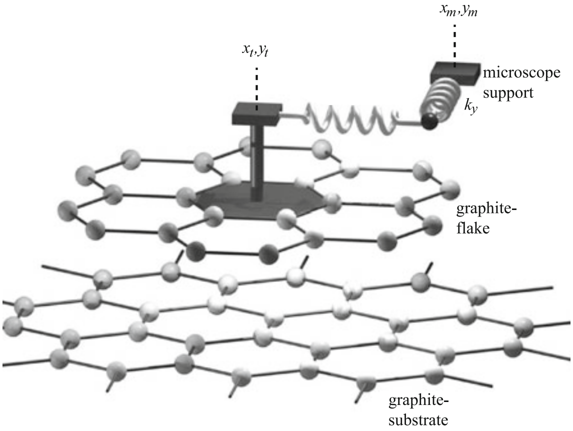

Fig. 8.3 Illustration of the modified Tomlinson model used in our calculations. A rigid graphite flake consisting of N carbon atoms (here $N = 24$) is connected by an x-spring and a y-spring to the support of the microscope. The support is moved in the x-direction. The substrate is modelled as a rigid, infinite, single layer of graphite. From [26]

As expected, the friction force was maximal if the misfit angle Φ was zero (or a multiple of 60°). For these orientations, the friction force increased linearly with the number of atoms N in the flake. In order to compare all different flake sizes for the same fixed total interaction between the flake and the surface, the potential amplitude per atom V_0 was lowered with increasing flake size such that the calculated friction force with the flake and substrate in registry was the same for all flakes, namely 265 pN at 0° pulling direction, between the values measured experimentally at misfit angles of 0° and 60°.

The effective interaction potential energy surface (PES) for the flake as a whole V_{int}^{flake} is shown in Fig. 8.4a for matching lattices ($\Phi = 0°$) for a flake size of $N = 96$. The small grey areas overlayed on the PES are the flake positions recorded in the 'forward' scan direction, during the 3 nm × 3 nm scan, parallel to the x-axis ($\Theta = 0°$). In Fig. 8.4a, the flake is only found in limited regions, slightly displaced to the upper right with respect to the minima of the PES. Also shown are flake pathways for three separate scan lines. During the scanning process the flake moves continuously through the grey 'sticking' regions, while force is built up in the spring. From the end of such a region it jumps (slips) to the beginning of the next sticking region. When the 96-atom flake is misaligned by 7°, the calculated lateral forces become small and for most trajectories the average lateral force, i.e. the friction

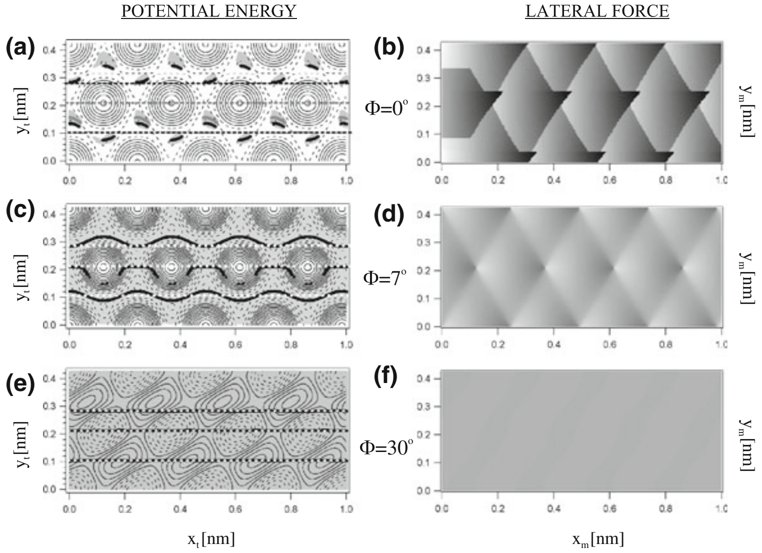

Fig. 8.4 Total potential energy surfaces and lateral force images (1.0 nm × 0.426 nm), calculated in the forward x-direction for a symmetric, 96-atom graphite flake sliding over a graphite substrate, for misfit angles $\Phi = 0°$ (**a**, **b**), $\Phi = 7°$ (**c**, **d**) and $\Phi = 30°$ (**e**, **f**). The *grey* scale in the lateral force images corresponds to the range [−1.04, 0.63] nN. For this range, **b** has maximal contrast. The *grey areas* in the potential energy *contour plots* denote positions that were visited by the flake. The *black lines* denote pathways of the flake during single scan lines of the support. From [26]

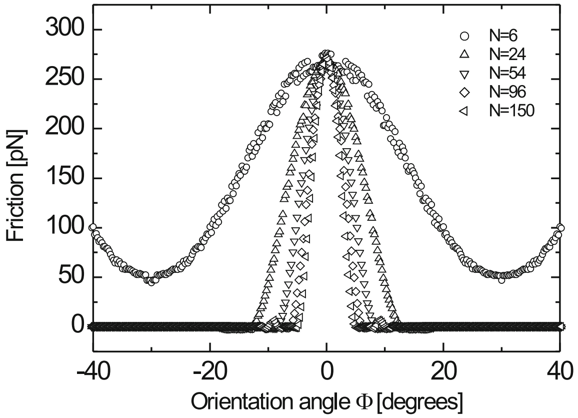

Fig. 8.5 Friction force as a function of the orientation angle for different symmetric graphite flakes ranging in size from 6 to 150 atoms, sliding over a graphite substrate. The potential amplitude per atom has been chosen such that all flakes share the same maximum friction value of 265 pN at $\Phi = 0°$. From [26]

force, vanishes completely within the precision of the calculation. The corrugation of the PES has decreased with respect to the situation at $\Phi = 0°$ and the regions addressed by the flake have merged, indicating that the flake moves continuously through most of the PES.

If the misalignment between the 96-atom flake and the substrate is further increased to 30°, the corrugation of the PES becomes so low that the pathway of the flake through the PES is identical to that of the support, within the precision of the calculation. The flake-graphite contact is now completely superlubric.

Figure 8.5 displays the computed friction force as a function of the misfit angle Φ, for five symmetric flakes with different sizes. We find an angular region with high friction around 0°, repeating every 60° due to the rotational symmetry of the flakes. At intermediate angles, near-zero friction is calculated, except for the 6-atom flake, for which the friction drops to 52 pN. These numerical calculations confirm the simple geometrical estimate, mentioned above, the best fit being produced by a flake with a size of $N = 96$ atoms. Further calculations showed that the shapes of the peaks in Fig. 8.5 also depended on the shapes of the flakes, the best fit to the experimental data being obtained for a symmetric flake, as shown by the curve in Fig. 8.2.

8.2.2 *The Role of the Normal Force*

As is clear from the description in Sect. 8.1.1, sliding without instabilities is possible also in the case of a single-atom contact or a contact between two commensurate lattices, provided that γ is smaller than 1. The required reduction of V_0 can be achieved by making the normal force sufficiently small, with which the tip is pressed against the substrate. In case of an attractive tip-substrate interaction, this may even require a negative external force, i.e. pulling the tip. This approach has been demonstrated recently by Socoliuc et al. In their FFM experiment, a silicon tip was scanned over a NaCl surface along the (100) direction in UHV. The observed force loops showed excellent agreement with the transition to frictionless sliding that is predicted by the one-dimensional Prandtl-Tomlinson model. As γ approached unity at a normal force of $F_N = -0.47$ nN, the area enclosed in the friction loop and, thus, the energy dissipated in a cycle reduced to zero and the tip was observed to slide over the NaCl surface without stick-slip motion. At that point the lateral force still showed slightly distorted sinusoidal variations with the periodicity of the surface lattice, but the average force was zero (Fig. 8.6c).

Following the original definition by Hirano and Shinjo [14], we should not refer to this form of near-frictionless sliding at low (or even negative) normal forces as superlubricity, since it does not involve the cancellation between lateral forces on individual atoms in the contact resulting from a mismatch between the two contacting surface lattices. By contrast, in the case of superlubricity, the normal force can be made surprisingly high [25]. We expect that the natural limit in the normal force, or rather contact pressure, will be that a new energy dissipation channel is introduced when the contact pressure is made high enough to induce noticeable lateral elastic deformations in the two contacting surfaces. In the case of such deformations, we can no longer describe the situation as that of two translating, rigid bodies [17]. In addition, the contact will then carry a rapidly shifting deformation pattern that one may view as a lattice of dislocation lines. Moving this pattern involves the combination of breaking atoms out of registry on one side of these lines and the popping of atoms back into registry on the other side. As these changes in atomic

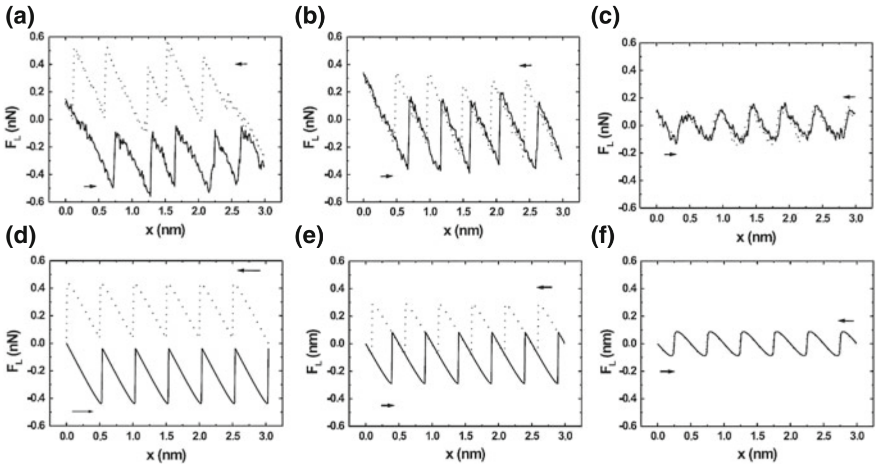

Fig. 8.6 Friction force loops of a Si tip sliding along the (100) direction of NaCl at **a** $F_N = 4.7$ nN, **b** $F_N = 3.3$ nN, and **c**, **a** $F_N = -0, 47$ nN. Prandtl-Tomlinson calculation with **d** $\gamma = 5$, **e** $\gamma = 3$, and **f** $\gamma = 1$. Reprinted from [27] with permission by A. Socoliuc and E. Gnecco

positions are no longer rigidly connected, much of the energy released on one side will not be re-invested on the other side and will be lost in the form of heat (phonons).

8.3 The Role of Temperature

Our discussion in the previous sections has been presented in terms of the classical mechanics of the sliding system, combined with the assumption of instantaneous loss of the excess energy during each slip event. These elements form the basis of the Tomlinson model that was used to fit the data in Fig. 8.2. One of the obvious simplifications in the Tomlinson model is the complete absence of effects due to the spontaneous thermal excitations that are present at finite temperatures. Such effects have been anticipated already by Prandtl in 1928 [10]. Here, we summarize how they lower the average friction force and may lead to a strongly modified type of sliding motion.

8.3.1 Weak Thermal Effects

It is easy to see that thermal excitations will assist the tip in overcoming the energy barrier for sliding from one well in the potential energy surface to the next. One might expect this phenomenon to become noticeable only when the amplitude of the potential V_0 (see 8.1 and 8.2) and, thus, the energy barriers would be limited to only a few times the thermal energy $k_B T$. However, one should realize that the tip moves in the *combined* potential of its interaction with the surface and its interaction with the spring that connects it to the moving support. Within the Tomlinson model the tip remains stuck in one well of this combined potential until the spring is sufficiently extended that the energy barrier to the next well vanishes, at which point the system is unstable and the tip necessarily slips into the next well. This means that even when the barrier to the next well starts out at a high value, it decreases continuously to zero while the spring is being stretched. This implies that thermal excitations will *always* play a role, since the stick part of the stick-slip cycle always contains a portion during which the barrier is sufficiently low with respect to $k_B T$ that it can be overcome by a thermally activated jump. This so-called pre-critical jump somewhat lowers the maximum lateral force that is exerted by the spring and thus reduces the friction force. The effect depends weakly on the sliding velocity because at lower velocities there is time for more attempts of the system to thermally overcome each barrier, which should make friction reduce more. It is easy to provide an estimate of this reduction in the friction force. Due to the exponential nature of the thermal excitations there is a range of sliding velocities over which the friction force is expected to increase proportionally with the logarithm of the sliding velocity v [28–30] or with $(\log v)^{2/3}$ [31]. Such a weak dependence of friction on sliding velocity has indeed been observed experimentally [30, 32, 33].

8.3.2 Strong Thermal Effects: Thermolubricity

As the measurements in Fig. 8.2 show, the rotation angle Φ of the graphite flake with respect to the graphite substrate determines the amplitude of the potential V_0 and can tune it anywhere between a high value of γ, at which there is strong friction, and low values $\gamma < 1$ that result in superlubricity. If the spring coefficient of the sensor k is low, as was the case in the measurements of Fig. 8.2, the transition to superlubricity takes place at a comparatively low value of the potential amplitude V_0. For example, at a typical (low) spring coefficient of $k = 1$ N/m and a typical lattice constant of $a = 0.25$ nm the transition to superlubricity is at a potential amplitude of only 10 meV, which is lower than the thermal energy at room temperature of 25 meV. This implies that for a contact that is close to superlubricity the role of thermal excitations will be much more dramatic than that described in the previous section. Rather than to merely facilitate the jumps that were bound to happen anyway (pre-critical jumps), thermal excitations are now sufficient to efficiently promote the system over all barriers, both to the next well(s) and to the previous one(s) [28]. As a result, the tip will conduct a random walk over the surface, its average position following the slow translation of the support. The stochastic nature of this driven diffusion of the tip is characterized by rapid force variations that replace the periodic stick-slip character, typical for higher γ values. The average lateral force, i.e. the observed friction force, is strongly reduced by these thermal jumps. It is this behavior for which we have proposed the term *thermolubricity* [34].

Figure 8.7 shows two selected force loops measured between a graphite substrate and a tungsten tip (dressed with a graphite flake) for two relative orientations, corresponding to two different values of γ. While the force loop for the higher γ still displays recognizable stick-slip behavior, the force variations at the lower γ value are almost completely stochastic. Note that the average friction force of the lower loop is close to zero, although γ is still well above unity, i.e. the system is not yet superlubric. These qualitative features agree well with the thermolubricity scenario. A stronger test is a quantitative confrontation of these observations with numerical calculations of thermolubricity. In these calculations we describe the surface potential as a one-dimensional sine function (8.1) to which we add the potential due to the interaction with the spring, $\frac{1}{2}k(x_t - x_m)^2$. If $\gamma < 1$ this combined potential shows only a single minimum for every position x_m of the support and the sliding is frictionless (superlubricity). When $\gamma > 1$ the combined potential shows several wells. Rather than to calculate individual trajectories or concentrate on average behavior, we describe the process in terms of the probabilities p_i for the tip to reside in each well i at every point in time. These probabilities evolve according to a simple set of continuity equations of the type:

$$v\frac{dp_i}{dx_m} = -(r_i^+ + r_i^-)p_i + r_{i-1}^+ p_{i-1} + r_{i+1}^+ p_{i+1}, \tag{8.3}$$

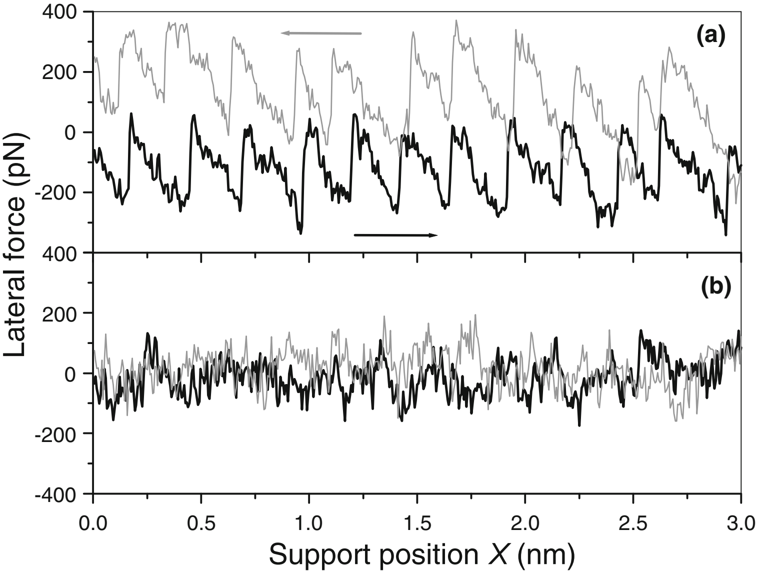

Fig. 8.7 Characteristic lateral force loops measured with a tungsten tip (with a graphite flake) on a graphite substrate at two different relative orientations, corresponding to **a** $\gamma = 5.0$ and **b** $\gamma = 2.5$. After [34]

where the role of time is played by the coordinate of the support $x_m = vt$. The rates r_i^+ and r_i^- of jumps from well i to the right and to the left are calculated according to the Arrhenius law:

$$r_i^{\pm} = r_0 \exp(-\frac{\Delta E_i^{\pm}}{k_B T}). \tag{8.4}$$

Here, $\Delta E_i^{\pm}$ are the energy barriers from well i to the next well and to the preceding one. The locations and heights of these barriers depend on the support position x_m. The prefactor r_0 is the frequency of attempted jumps, which is treated as a fitting parameter (see below). Equation (8.3) can be solved analytically in the limit of very strong thermolubricity, i.e. low velocities v, low amplitudes of the potential V_0 and/or high temperatures T. For other conditions the probabilities need to be evaluated numerically.

Figure 8.8 demonstrates that for $\gamma > 1$ the experiments presented before, probing the lateral forces between a graphite-decorated tungsten tip and a graphite substrate, clearly exhibit thermolubricity. For each value of the relative strength of the potential γ the experimental data fall significantly below the dashed curve, which is the friction force expected according to the Tomlinson model. The full curves show the results obtained from (8.3) for the values of T, v, a, and k taken from the experiment and for four different values of the attempt frequency r_0. Like the experiment, the theoretical curves fall below the curve for the Tomlinson model. The second curve, for $r_0 = 1.6$ kHz, provides an excellent fit to the experiment. This frequency is in the

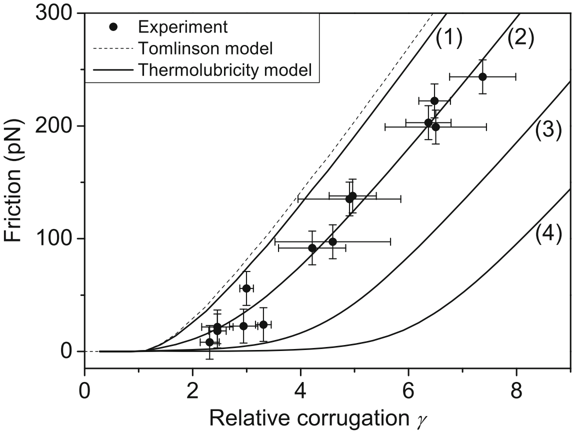

Fig. 8.8 Friction force as a function of relative surface corrugation γ. Experiments for a graphite substrate and a tungsten tip with a graphite flake are compared with numerical solutions of (8.3) for $v = 30\,\text{nm/s}$, $a = 0.25\,\text{nm}$, $k = 1.8\,\text{N/m}$ and $T = 290\,\text{K}$ and for $v/ar_0 = 7.53 \times 10^{-n}$ with (from *left* to *right*) $n = 1, 2, 3, 4$. Experiment and calculations all fall well below the *dashed curve*, which shows the corresponding result from the Tomlinson model, i.e. the friction force in absence of thermal excitations. After [34]

order of the eigenfrequency of the employed Tribolever sensor. Although this may not seem very surprising, further work will be necessary to resolve why the much higher vibration frequencies of the apex of the tip seem not to dominate the value of r_0.

8.4 Other Manifestations of Superlubricity and Thermolubricity

8.4.1 Lubrication by Graphite and Other Lamellar Solids

Graphite is a popular solid lubricant that is usually applied in the form of flaky powder. Several other layered materials also show excellent lubricating properties, for example MoS_2 and Ti_3SiC_2. Traditionally, the good lubrication by these materials is ascribed to the weak interaction between adjacent layers [35]. However, the intuitive idea that this would lead to easy shear cannot be correct, since it would still require the simultaneous rupture of all bonds in a plane, which involves a tremendously high energy, even for the weakly interacting layers in graphite [36]. Based on the lateral force measurements discussed in this chapter it seems natural to add the extra element of superlubricity and possibly also that of thermolubricity to the low-friction scenario of graphite. As argued above, the easy shear cannot take place *within* individual pieces of graphite, but it can occur *between* flakes of graphite since in a lubrication film flakes will be oriented randomly with respect to each other, which introduces the mismatch required for superlubricity and thermolubricity for almost all graphite-graphite contacts. It is known that when metals are lubricated by graphite under ambient conditions, the oxide layers on the metals tend to fix some of the graphite to the metal, leading to a smooth transfer film [37], which would indeed concentrate most of the shear motion within the film of graphite flakes, rather than between the graphite and the metal surfaces. In a practical sliding geometry, the normal and shear forces will not be carried by a single, macroscopic flake-flake contact but it will be distributed over a large ensemble of simultaneous microcontacts between flakes, most of which will be slippery due to superlubricity or thermolubricity, while only a small fraction will be in temporary registry.

Strong support for the suspicion that it is the slipperiness of misoriented flakes that makes the friction low when macroscopic contacts are lubricated by layered solids comes from transmission electron microscopy observations by Martin et al. on MoS_2 [20]. TEM inspection of wear particles harvested from a MoS_2 lubrication film that had been exposed to sliding friction revealed Moiré patterns characteristic for superimposed flakes that were rotated with respect to each other around their c-axis.

8.4.2 Lubrication by Diamond-Like Carbon and Related Coatings

We also briefly speculate about the extremely good lubricating properties of diamond-like carbon (DLC) coatings and related, carbon containing materials and propose that it is again the superlubricity and thermolubricity of graphite that might be responsible. During the running-in phase, some of the DLC coating may be transformed into graphite and remain loosely bound to the DLC film. A relatively small amount of graphitized material should be sufficient to decorate all asperities and thus dominate the shear response. The main role of the DLC film would thus be to provide the material (carbon) and the conditions (e.g. through its hardness) necessary to produce small amounts of graphite. An essential element of this scenario is that it is self-terminating. The high friction forces at the beginning of run-in provide local pressures and temperatures that should be high enough to shear off carbon from the DLC film and graphitize it. Once it has been formed, the graphite dramatically reduces friction, so that the local shear stresses on the DLC film are too low to continue wearing off the film and graphitizing it. It has indeed been demonstrated that under sliding conditions, a graphitized tribolayer is formed on top of diamond-like carbon (DLC) coatings, which goes hand in hand with the decrease of the friction coefficient during run-in [38].

8.4.3 Lubrication by Fullerenes and Carbon Nanotubes

Fullerenes show very low friction when they are oriented in an incommensurate fashion. Miura et al. [39] have constructed a molecular ball bearing by placing a monolayer of C_{60} molecules between two graphite sheets of $1\,\text{mm}^2$. When they moved the upper graphite flake with an FFM tip, they observed that the forward and backward traces were identical and no energy dissipation was measurable up to normal loads of more than 100 nN. Surprisingly the lateral force traces still showed sawtooth-like force variations which are typical for instabilities and thus significant friction should be expected. Therefore the Prandtl-Tomlinson model apparently is not able to describe the low friction behavior of this system. Falvo et al. [40, 41] manipulated carbon nanotubes (CNTs) on a graphite surface using the tip of an FFM. They observed that the CNTs changed from sliding to rolling motion, depending on the orientation of the tubes on the substrate. The rolling motion of the CNTs in the case of a commensurate contact was found to require a higher lateral force than the sliding motion of the CNTs in the case of an incommensurate contact. Cumings and Zettl [42] have used a TEM to estimate the friction force between two tubes of a multiwall carbon nanotube (MWNT) in the direction of the long axis. They pulled the core tube out of the outer tube and calculated the friction force from the retraction time, which was below 1.5×10^{-5} nN/atom.

Nanoparticles form another interesting model system to study the friction between two finite surfaces. By deposition of Sb particles on graphite and MoS_2, Ritter et al. [43] have created incommensurate contacts of various sizes. At a certain size the particles undergo a transition from amorphous to crystalline and at that point an increase in friction was observed. Although their friction was low, the amorphous particles were found not to be completely superlubric in air [44]. For future applications in superlubric meso- or macroscopic mechanical systems it is very important to learn why superlubricity is not seen in this case.

8.5 Concluding Remarks

In this chapter we have reviewed friction force microscopy experiments on extremely low friction and their interpretation in terms of lattice mismatch effects (superlubricity) and effects due to thermal excitations (thermolubricity). The prospect of exploiting these effects in practical applications, for example in nano- and micro-electro-mechanical systems (NEMS and MEMS) is exciting. The examples of excellent lubrication by graphite and other layered materials and by modern, carbon containing coatings such as DLC strongly suggest that these effects can indeed manifest themselves on macroscopic length scales and under realistic loading conditions.

It is evident that many questions have not been addressed in the studies reviewed here on nanoscale contacts. Similarly, many aspects remain to be explored on the way from a single, nano-contact under modest loading pressures to a large ensemble of larger contacts with possibly higher loading. An example is the effect of the load-dependent elastic deformations that may be expected to undermine the slipperiness, as mentioned in Sect. 8.2.2.

Another important issue is whether we can evoke superlubricity- and thermolubricity-based slipperiness also on other materials than layered solids such as graphite and related materials. Simulations for copper sliding over copper [16] suggest that there is no fundamental reason against this possibility, which is therefore demanding to be examined.

Acknowledgments The authors are grateful to a large number of people for their valuable contributions to the work reviewed in this chapter. In particular we mention J.A. Heimberg for the design and construction of the friction force microscope, K.B. Jinesh and N. Pradeep for performing part of the experiments and analysis, S. Yu. Krylov for setting up the theory of thermolubricity and G.S. Verhoeven and H. Valk for numerical calculations of superlubricity and thermolubricity. The work presented in Sects. 8.2.1 and 8.3.2 is part of the research program of the "Stichting voor Fundamenteel Onderzoek der Materie (FOM)" and was made possible by financial support of the "Nederlandse Organisatie voor Wetenschappelijk Onderzoek (NWO)".

References

1. C.M. Mate, G.M. McClelland, R. Erlandsson, S. Chiang, Phys. Rev. Lett. **59**, 1942 (1987)
2. S. Fujisawa et al., J. Vac. Sci. Technol. B **12**, 1635 (1994)
3. S. Morita, S. Fujisawa, Y. Sugawara, Surf. Sci. Rep. **23**, 1 (1996)
4. R. Bennewitz et al., Phys. Rev. B **60**, R11301 (1999)
5. G.J. Germann et al., J. Appl. Phys. **73**, 163 (1993)
6. R.J.A. van den Oetelaar, C.F.J. Flipse, Surf. Sci. Lett. **384**, L828 (1997)
7. R.W. Carpick, Q. Dai, D.F. Ogletree, M. Salmeron, Tribol. Lett. **5**, 91 (1998)
8. L. Howald et al., J. Vac. Sci. Technol. B **12**, 2227 (1994)
9. R. Lüthi et al., J. Vac. Sci. Technol. B **14**, 1280 (1996)
10. L. Prandtl, ZS f. angew. Math. u. Mech. **8**, 85 (1928)
11. G.A. Tomlinson, Phil. Mag. S.7 **7**, 905 (1929)
12. S. Aubry, The New Concept by Breaking of Analyticity in a Crystallographic Model, in *Solitons and Condensed Matter Physics*, ed. by A.R. Bishop, T. Schneider (Springer, Berlin, 1979), p. 264
13. S. Aubry, Phys. D **7**, 240 (1983)
14. K. Shinjo, M. Hirano, Surf. Sci. **283**, 473 (1993)
15. M. Hirano, K. Shinjo, Phys. Rev. B **41**, 11837 (1990)
16. M.R. Sørensen, K.W. Jacobsen, P. Stoltze, Phys. Rev. B **53**, 2101 (1996)
17. M.H. Müser, Europhys. Lett. **66**, 97 (2004)
18. M. Hirano, K. Shinjo, R. Kaneko, Y. Murata, Phys. Rev. Lett. **67**, 2642 (1991)
19. J.S. Ko, A.J. Gellman, Langmuir **16**, 8343 (2000)
20. J.M. Martin, C. Donnet, T. LeMogne, T. Epicier, Phys. Rev. B **48**, 10583 (1993)
21. M. Hirano, K. Shinjo, R. Kaneko, Y. Murata, Phys. Rev. Lett. **78**, 1448 (1997)
22. T. Zijlstra et al., Sens. Actuators A **84**, 18 (2000)
23. M. Dienwiebel et al., Rev. Sci. Instrum. **76**, 043704 (2005)
24. M. Dienwiebel et al., Phys. Rev. Lett. **92**, 126101 (2004)
25. M. Dienwiebel et al., Surf. Sci. **576**, 197 (2005)
26. G.S. Verhoeven, M. Dienwiebel, J.W.M. Frenken, Phys. Rev. B **70**, 165418 (2004)
27. A. Socoliuc, R. Bennewitz, E. Gnecco, E. Meyer, Phys. Rev. Lett. **92**, 134301 (2004)
28. T. Baumberger, P. Berthoud, C. Caroli, Phys. Rev. B **60**, 3928 (1999)
29. C. Caroli, P. Nozières, in *Physics of Sliding Friction, Vol. 311 of NATO ASI Series E: Applied Sciences*, ed. by B.N.J. Persson, E. Tosatti (Kluwer, Dordrecht, 1996), p. 27
30. E. Gnecco et al., Phys. Rev. Lett. **84**, 1172 (2000)

31. Y. Sang, M. Dubé, M. Grant, Phys. Rev. Lett. **87**, 174301 (2001)
32. E. Riedo et al., Phys. Rev. Lett. **91**, 084502 (2003)
33. K.B. Jinesh, J.W.M. Frenken, Phys. Rev. Lett. **96**, 166103 (2006)
34. S.Y. Krylov et al., Phys. Rev. E **71**, 065101(R) (2005)
35. W. Bragg, *An Introduction to Crystal Analysis* (G.Bell and Sons Ltd., London, 1928)
36. G.I. Finch, Proc. Phys. Soc. A **63**, 785 (1950)
37. F.P. Bowden, D. Tabor, *The Friction and Lubrication of Solids* (Clarendon Press, Oxford, 1964)
38. Y. Liu, A. Erdemir, E.I. Meletis, Surf. Coat. Technol. **86–87**, 564 (1996)
39. K. Miura, S. Kamiya, N. Sasaki, Phys. Rev. Lett. **90**, 055509 (2003)
40. M.R. Falvo et al., Nature **397**, 236 (1999)
41. M.R. Falvo, J. Steele, R.M. Taylor II, R. Superfine, Phys. Rev. B **62**, R10665 (2000)
42. J. Cumings, A. Zettl, Science **289**, 602 (2000)
43. C. Ritter, M. Heyde, B. Stegemann, K. Rademann, Phys. Rev. B **71**, 085405 (2005)
44. C. Ritter, Private communication